

# Exploring the limiting timing resolution for large volume CZT detectors with waveform analysis

L.J. Meng\*, Z. He

*Department of Nuclear Engineering and Radiological Sciences, University of Michigan, 1906 Cooley Building,  
2355 Bonisteel Blvd., Ann Arbor MI 48109, USA*

Received 8 March 2005; received in revised form 22 April 2005; accepted 25 April 2005  
Available online 5 July 2005

---

## Abstract

This paper presents a study for exploring the limiting timing resolution that can be achieved with a large volume 3-D position sensitive CZT detector. The interaction timing information was obtained by fitting the measured cathode waveforms to pre-defined waveform models. We compared the results from using several different waveform models. Timing resolutions, of  $\sim 9.5$  ns for 511 keV full-energy events and  $\sim 11.6$  ns for all detected events with energy deposition above 250 keV, were achieved with a detailed modeling of the cathode waveform as a function of interaction location and energy deposition. This detailed modeling also allowed us to derive a theoretical lower bound for the error on estimated interaction timing. Both experimental results and theoretical predications matched well, which indicated that the best timing resolution achievable in the  $1\text{ cm}^3$  CZT detector tested is  $\sim 10$  ns. It is also showed that the correlation between sampled amplitudes in cathode waveforms is an important limiting factor for the achievable timing resolution. © 2005 Elsevier B.V. All rights reserved.

**Keywords:** Timing resolution; Large volume 3-D position sensitive cz; Waveform analysis

---

## 1. Introduction

Over the past several years, substantial efforts have been made in developing large volume 3-D position sensitive CZT detectors for detecting gamma-rays and other energetic particles [1,2]. These devices have shown great potential for gamma-ray imaging and spectroscopy. For exam-

ple, an energy resolution of  $\sim 0.7\%$  at 662 keV for single interaction events and a 3-D position resolution of  $< 1$  mm FWHM have been experimentally demonstrated with a detector of  $2\text{ cm}^3$  in size. These gamma-ray sensors also have the capability of processing multiple simultaneous interactions, so that imaging can be realized with a single detector working as a Compton camera. The combination of high-energy resolution, high spatial resolution and good stopping power offers an excellent detector option for next generation positron emission tomography (PET) systems.

---

\*Corresponding author. Tel.: +1 734 7645285.

E-mail address: [ljmeng@umich.edu](mailto:ljmeng@umich.edu) (L.J. Meng).

One of the challenges for using this detector for PET application is how to achieve a reasonable timing resolution. Traditional leading edge or constant fraction discrimination methods are less feasible due to the low signal-to-noise ratio (SNR) and significant time walk resultant from the low-charge carrier mobility. To overcome this difficulty, we tested an alternative approach that uses pulse waveform analysis to estimate interaction timing [3]. This method provided a great improvement in timing resolution with a large volume HgI<sub>2</sub> detector having similar configuration. The focus of this work is to explore the limiting timing resolution that can be achieved with large volume CZT sensors for detecting 511 keV gamma-rays.

## 2. Materials and methods

### 2.1. Timing estimation in large volume 3-D CZT detectors

One of the most common ways to obtain timing information is to trigger on amplified signals. This scheme is, however, less feasible for large volume CZT detectors. The low mobility of charge carriers limits the achievable SNR on the shaping amplifier output. It is difficult to achieve a good timing resolution by triggering on such signals. Furthermore, interactions occur at different depths, between the anode and the cathode, would induce pulses with different peaking times. It leads to significant time walk when simple leading edge or constant fraction triggering methods are used. It is also experimentally demonstrated that even for interactions that occurred at the same location in the detector, the electron collection time may be fluctuating for several tens of nano-seconds [3]. This gives an extra uncertainty for the obtaining timing information using analogue triggering.

To overcome these difficulties, we explored an alternative approach that utilizes the cathode pulse waveform to estimate the interaction time directly. The idea is to fit the measured pulse waveform to pre-defined waveform models that is characterized by model parameters including interaction timing. We tested this approach with a  $10 \times 10 \times 10 \text{ mm}^3$

CZT detector. Detailed operating characteristics of this detector can be found in Ref. [4]. It has  $11 \times 11$  anode pixels of  $0.9 \times 0.9 \text{ mm}^2$  and a large continuous cathode on the opposite side. The detector was biased at  $-1400 \text{ V}$ . This detector offers an energy resolution of  $\sim 1\%$  at 662 keV and a 3-D position resolution of  $< 1 \text{ mm}$  FWHM. The depth of interaction can be estimated using the ratio between cathode and anode signal amplitudes, which we refer to as CAR in the following text. In this study, induced charge on an anode pixel and the planar cathode were readout individually using discrete pre-amplifiers (Amptek A250 [5]). An HP digital oscilloscope was used to digitize the outputs from the pre-amplifiers. It operates at a sampling rate of  $10^9$  samples/s with 8 bit precision. In order to determine the precise time of interaction, we also used a BaF<sub>2</sub> detector working in coincidence with the CZT sensor. An <sup>22</sup>Na point source was placed between these two detectors.

### 2.2. Using cathode waveform for timing estimation

For semiconductors with planar readout electrodes, the cathode waveforms can be approximated by Hecht relation [6]. If we include the charge trapping effect only and ignore the possible de-trapping effect, the induced charge on a planar electrode as a function of time  $t$  and for carriers of a single polarity is given by

$$w(t) = \begin{cases} \frac{eN_0\tau_f}{T_c} (1 - e^{-t/\tau_f}) & t < T_c \\ \frac{eN_0\tau_f}{T_c} (1 - e^{-T_c/\tau_f}) & t \geq T_c \end{cases} \quad (1)$$

where  $T_c$  is the time by which all free charge carriers are collected.  $N_0$  is the number of charge carriers initially generated and  $\tau_f$  is the mean-free time of the carriers. An example of the measured cathode pulse waveform resulted from a 511 keV full energy deposition in the CZT detector is shown in Fig. 1. The interaction timing is determined by finding the tuning point as shown in the figure.

In our previous work, we have experimentally demonstrated that a good timing resolution can be obtained by fitting the measured pre-amplifier pulse waveforms to waveform models based on

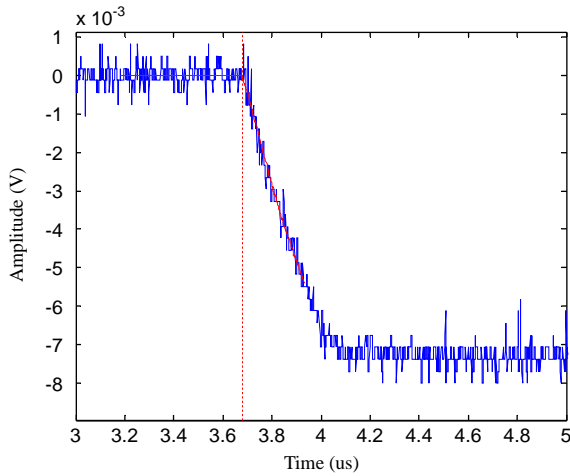


Fig. 1. An example of measured cathode pulse waveform for an event that occurred close to the cathode. The red solid line is the waveform model that fits best to this waveform and the vertical dotted line indicates the interaction timing for this event.

Hecht relation [3]. However, this approach has several limitations. The least-squares fitting process normally requires many iterations for finding the model parameters. This involves a relatively large number of floating point operations for each detected event and therefore sets an upper limit on the event rate that can be handled with realistic hardware. For this reason, it is important to reduce the number of parameters in the model. The number of floating point operations is proportional to the number of model parameters if one assumes that the same number of iterations were to be used. Secondly, as a simplified waveform model, Hecht relation does not take into account details such as inhomogeneity of internal electric field, material non-uniformity and irregular weighting potential functions. In our previous work, we analyzed the uncertainty associated with the measured waveforms. It showed that the fluctuation due to random charge generation and trapping/de-trapping processes is negligible compared to the readout electronic noise. We therefore assumed (in the previous study) that the uncertainty on the measured waveform can be modeled by Gaussian white noise, dominated by the readout electronic noise. As we will show later in this paper, this is an oversimplified noise model. The

measured covariance of the actual waveforms showed significant correlation between waveform amplitudes sampled at different times. Ignoring such correlation would degrade the accuracy for timing estimations.

The key to achieve the optimum timing resolution is to develop an accurate statistical description of the detector's response. To obtain this information, we carried out a detailed analysis of the expected detector response to gamma-rays interacting at different locations and with different energy depositions. Given the 3-D position information provided by the detector, we can identify events from a specific interaction location and with 511 keV full energy deposition. The mean waveform for these events were obtained by averaging over measured waveforms lined up at the same starting time:

$$\bar{w}_{511 \text{ keV}}(t) = \frac{\sum_{i=1}^N w(t - T_i)}{N} \quad (2)$$

where  $T_i$  is the true interaction timing obtained from the BaF<sub>2</sub> coincidence detector.  $\bar{w}_{511 \text{ keV}}(t)$  is the mean waveform resulting from an 511 keV energy deposited at this given location, assuming that the interaction occurred at  $t = 0$ . From this, we can write the expected waveform for a single interaction at the same location by

$$\bar{w}(e, z_0, t_0) = \begin{cases} z_0 & t \leq t_0 \\ e\bar{w}_{511 \text{ keV}}(t - t_0) + z_0 & t > t_0 \end{cases} \quad (3)$$

where  $z_0$  is the DC offset on the pre-amplifier output right before the interaction time  $t_0$ . To account for interactions at the same depth but with different energy depositions, we introduced a factor  $e$  to allow the slope of the cathode waveform changing with energy deposition. Note that the interaction location is not explicitly shown in Eq. (3). When using the large volume 3-D CZT detector, one can find the interaction location(s) for each event (including that with multiple interaction sites) in real time. This unique capability is detailed in Refs. [1,2]. Based on this information, we select an appropriate mean waveform and then use the fitting process to find interaction timing. This method is called “indexed

waveform matching”, which will be discussed later in this paper.

The covariance of measured waveforms is defined by

$$\begin{aligned} \text{Cov}[w(t), w(t+u)] &= \int_{w(t)} \int_{w(t+u)} [w(t) - \bar{w}(t)] \\ &\times [w(t+u) - \bar{w}(t+u)] p[w(t), w(t+u)] \\ &\times dw(t) dw(t+u) \end{aligned} \quad (4)$$

where  $p[w(t), w(t+u)]$  is the joint probability density function for the waveform amplitudes sampled at time  $t$  and  $t+u$ . This covariance can be derived from the same data set if a sufficiently large number of events are collected. Since measured waveforms can be modeled closely with multivariate Gaussian distribution, knowing the mean and covariance of a measured waveform allows one to estimate the interaction timing,  $t_0$ , by maximizing the likelihood function

$$l \propto \exp\left\{-\frac{1}{2}[w - \bar{w}(e, z_0, t_0)]^T \Sigma^{-1} [w - \bar{w}(e, z_0, t_0)]\right\} \quad (5)$$

or equivalently minimizing the  $\chi^2$  term

$$\chi^2 = [w - \bar{w}(e, z_0, t_0)]^T \Sigma^{-1} \cdot [w - \bar{w}(e, z_0, t_0)] \quad (6)$$

where  $w$  is the measured waveform and  $\Sigma$  is the covariance matrix corresponding to  $w$ . This maximization/minimization problem can be solved with standard algorithms such as Levenberg–Marquardt method [7].

### 2.3. Theoretical limits on timing resolution

Given an accurate system model, the minimum achievable error for estimating interaction timing can be derived as the Cramer–Rao Bound (CRB) for unbiased estimators [8]. Suppose that the parameters to be estimated are  $\theta = [\theta_1, \theta_2, \theta_3, \dots, \theta_M]^T$  (an  $M \times 1$  vector) and the mean waveform is  $\bar{w}(\theta) = [\bar{w}_1(\theta), \bar{w}_2(\theta), \dots, \bar{w}_N(\theta)]^T$ , the Fisher Information Matrix (FIM) is defined by

$$\mathbf{J}(\theta) = \left( \frac{\partial \bar{w}(\theta)}{\partial \theta} \right)^T \Sigma^{-1} \left( \frac{\partial \bar{w}(\theta)}{\partial \theta} \right) \quad (7)$$

where

$$\left( \frac{\partial \bar{w}}{\partial \theta} \right)^T = \begin{pmatrix} \frac{\partial \bar{w}_1(\theta)}{\partial \theta_1} & \frac{\partial \bar{w}_2(\theta)}{\partial \theta_1} & \dots & \frac{\partial \bar{w}_M(\theta)}{\partial \theta_1} \\ \frac{\partial \bar{w}_1(\theta)}{\partial \theta_2} & \frac{\partial \bar{w}_2(\theta)}{\partial \theta_2} & \dots & \frac{\partial \bar{w}_M(\theta)}{\partial \theta_2} \\ \vdots & \vdots & \ddots & \vdots \\ \frac{\partial \bar{w}_1(\theta)}{\partial \theta_N} & \frac{\partial \bar{w}_2(\theta)}{\partial \theta_N} & \dots & \frac{\partial \bar{w}_M(\theta)}{\partial \theta_N} \end{pmatrix}. \quad (8)$$

Each row of  $\mathbf{J}$  is the expected change of the mean waveform due to a unit change in the value of the corresponding model parameter. The minimum achievable error (covariance) on the estimated model parameters  $\hat{\theta}$  is simply obtained by

$$\text{Cov}(\hat{\theta}) \geq \mathbf{J}^{-1}. \quad (9)$$

This method has been used by Hero and Clinthorne et al for quantifying the accuracy of timing estimation based on BGO scintillation detectors [9,10]. In that study, the estimation error predicted by the CRB is much smaller than what achieved in reality. The reason for this discrepancy is that the signal from the scintillation detector is dominated by the shot noise from the relatively small number of photoelectrons generated. This noise behavior is not correctly modeled in the assumption leading to the derivation of the CRB. In our case, the noise on the measured waveform is well-approximated with Gaussian distribution, we expect the CRB to be fairly close to the accuracy achievable in measurements.

## 3. Results

### 3.1. Using C/A ratio and anode amplitude as index

For each interaction, we can use the combination of the CAR and the anode amplitude as an index to pick up the most likely waveform model. So the fitting process always starts from an initial guess that is very close to the ML solution. It does not need to search through a large number of possible combinations of model parameters. This helps to achieve an optimal computational efficiency and also results in more reliable timing estimation. Fig. 2 shows a scattered plot of measured anode amplitudes

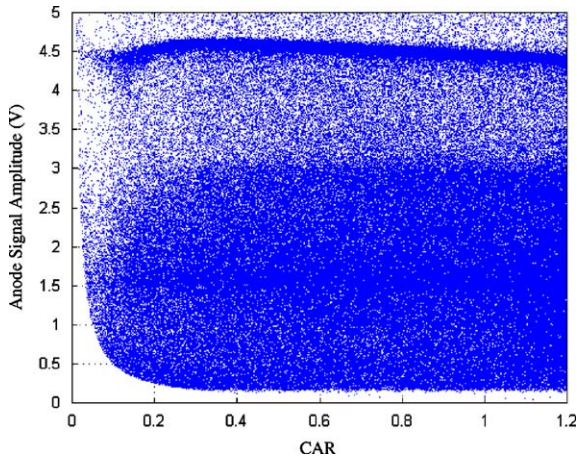


Fig. 2. Scattered plot of anode signal amplitude as a function CAR (interaction depth). Source used:  $^{22}\text{Na}$ .

versus cathode-to-anode ratio (or interaction depth). Ideally, the system response function should contain the mean waveform and the covariance on the measured data for each possible combination of CAR and anode amplitude, or equivalently the combination of energy deposition and interaction depth in the detector.

### 3.2. Characteristics of cathode pulse waveforms

#### 3.2.1. Mean waveforms

In order to derive the mean waveform, we collected a large data set that allowed us to make a scattered plot (Fig. 2) with a reasonable density of events. We then subdivide the plot into tiny 2-D boxes. An example is shown in Fig. 3, in which we divide the photopeak events with  $C/A$  ratios around 0.825 (relatively close to the cathode) into five boxes. We looked through all events falling into each of these small 2-D boxes. The average waveform for all events in Box 1 is shown in Fig. 4, along with the standard deviation of the measured waveforms around this mean. A comparison between the mean waveforms corresponding to the five boxes is shown in Fig. 5. It is worth noting that the mean waveforms for events in these five boxes are relatively uniform when electrons are relatively close to where they were generated (0–200 ns). When electrons are moving closer to

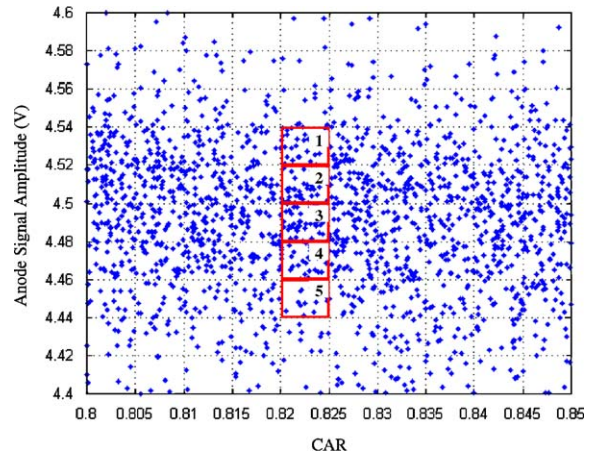


Fig. 3. Scattered plot of anode signal amplitude as a function CAR. Five sub regions across the photopeak area are indicated.

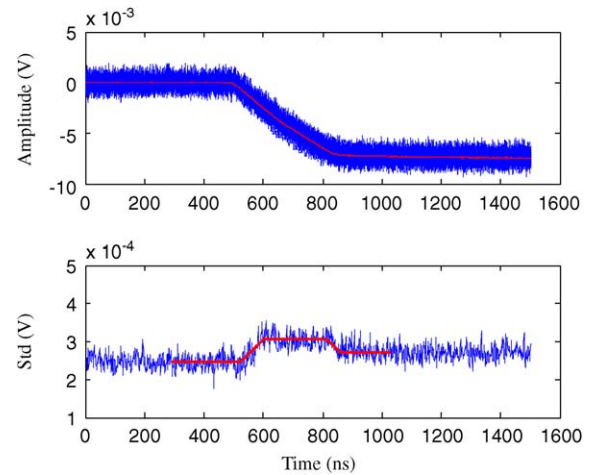


Fig. 4. Upper panel. Expected cathode waveform (solid line) derived by averaging all waveforms (overlapping curves) that fall into Box 1. Lower panel. standard deviation. The red solid line shown in the lower panel is the estimated standard deviation, which will be used later for deriving an approximated covariance matrix.

anode pixels, we start to see difference between the mean waveforms. Events from Box 1 tend to have shorter electron collection times and larger induced charge signals, whilst events from Box 5 had a  $\sim 30$  ns longer electron drifting time. This effect may be explained by the fact that anode pixels have a finite lateral dimension. When an electron



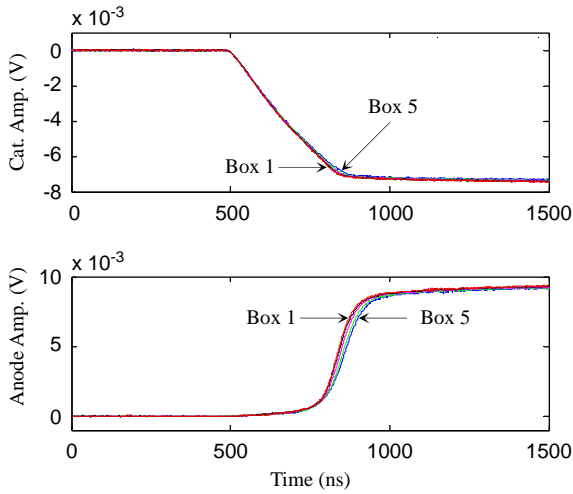


Fig. 5. A detailed comparison of the mean waveforms for events from the five boxes defined in Fig. 3.

cloud was generated below the center of the pixel, the trajectory of the electron cloud is almost a straight line perpendicular to the anode surface (the  $z$ -direction). If an electron cloud is generated close to the edge of the pixel, its trajectory will initially follow the  $z$ -direction and be bent toward the center of the pixel (by the potential difference between the collecting and non-collecting anodes) when moving close to the anode plane. This effect leads to not only longer electron drifting time, but also slightly lower charge collection efficiency due to the relatively low electric field strength near the non-collection anode. We expect that this non-uniformity on cathode pulse waveform to become more severe for interactions occur closer to the anode pixel ( $C/A$  ratio  $< 0.3$ ). This process was repeated for photopeak events with  $C/A$  ratios of  $\sim 0.2$  and  $\sim 1.0$ . A comparison of the resultant mean waveforms is shown in Fig. 6.

Note that for the same energy deposition, the slope of the cathode waveform is larger when interactions occurred closer to the cathode plane (Fig. 5). One possible explanation is that the assumption on planar geometry does not hold for this detector. The weighting potential for the cathode plane is not a linear function of the depth. The cathode acts like a big pixel rather than an infinitely large plane. This effect was not ac-

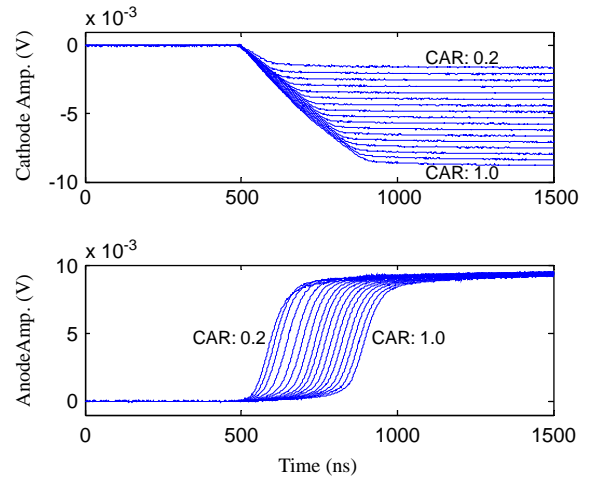


Fig. 6. Mean waveforms for 511 keV full-energy events occur at different depths.

counted for by the single exponential model shown in Table 1. This effect could also be due to the inhomogeneity of the electric field inside the detector.

### 3.2.2. Covariance of cathode waveforms

In our previous analysis [3], we assumed that the covariance matrix on the measured waveforms has a diagonal form, so that the uncertainties on waveform can be modeled as Gaussian white noise. In the fitting process (described in Ref. [3]), we used a covariance that has entries

$$\text{Cov}[w(t), w(t+u)] = 0 \quad \text{if } |u| > 0.$$

However, our experimentally measured covariance matrix is noticeably different from this model. First, the variances on the measured waveforms are not constant. It is increasing when electrons are drifting further away from their initial location. Secondly, the noise on the waveform amplitudes sampled at different times is clearly correlated, as indicated by the non-zero off-diagonal entries in the covariance matrix, as shown in Fig. 7. As a comparison, the simple Gaussian white noise model would lead to a delta function centered at 128 ns, with no other non-zero entries otherwise. As far as the fitting is concerned, this correlation indicates that although we may use all

Table 1  
Waveform models used in timing estimation

Waveform models	Definition	No. of model parameters
Optimum	$\bar{w}(t) = \begin{cases} z_0 & t \leq t_0 \\ e\bar{w}_{511 \text{ keV}}(t - t_0) + z_0 & t > t_0 \end{cases}$	3 ( $e, z_0, t_0$ )
Single exponential	$w(t) = \begin{cases} \lambda_1 t + \lambda_2 & t \leq t_0 \\ (\lambda_1 t + \lambda_2) + \lambda_3 \lambda_4 \left[ 1 - \exp\left(-\frac{t-t_0}{\lambda_4}\right) \right] & t > t_0 \end{cases}$	5 ( $\lambda_1, \lambda_2, t_0, \lambda_3, \lambda_4$ )
Linear	$w(t) = \begin{cases} \lambda_1 t + \lambda_2 & t \leq t_0 \\ \lambda_3 t + [(\lambda_1 - \lambda_3)t_0 + \lambda_2] & t > t_0 \end{cases}$	4 ( $\lambda_1, \lambda_2, t_0, \lambda_3$ )

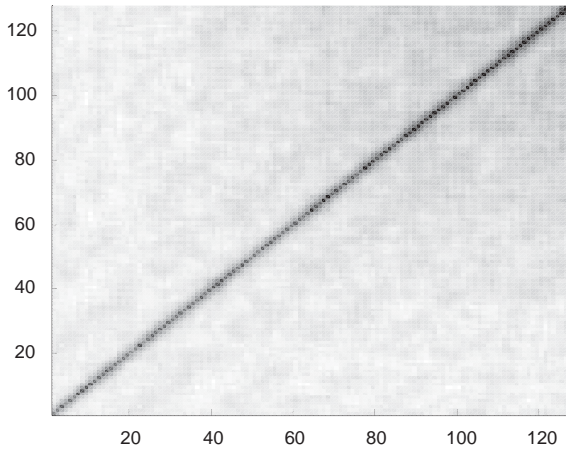


Fig. 7. Measured covariance matrix for waveform section corresponding to the first 128 ns after interaction.

the  $\sim 200$  points on the falling edge, many points included are redundant. The reduction in variance for timing estimation is not a linear function of the number of data points used in the fitting.

For both timing estimation and derivation of the CRB, we need to have a reasonably accurate covariance matrix  $\Sigma$ , which reflects the non-zero waveform covariance. In principle,  $\Sigma$  can be numerically evaluated by collecting a very large number of events. This is, however, difficult to do in reality because one would need to have a sufficiently large number of events falling into a tiny 2-D box in the scatter plot (Fig. 6) to minimize the error. In this study, we used a simplification for the covariance matrix. We assumed that the covariance matrix of the measured waveforms is

the sum of two matrices

$$\Sigma_{\text{total}} = \Sigma_{\text{electronic}} + \Sigma_{\text{transport}}, \quad (11)$$

where  $\Sigma_{\text{electronic}}$  is a diagonal matrix representing the Gaussian white noise of known amplitude and  $\Sigma_{\text{transport}}$  is the covariance matrix resultant from the random charge transport process. Although the exact cause for this correlation is difficult to determine, there are several effects that are known to contribute to  $\Sigma_{\text{transport}}$ . The random processes for carrier generation and trapping/de-trapping will introduce non-zero correlation. This effect should be relatively small, given the known electron trapping properties and mean ionization energy in CZT [3]. Detector material non-uniformity may result in charge carrier clouds, generated at the same location, to take slightly different routes when drifting toward readout electrodes. For these effects, the amplitude of the waveform at time  $t + u$  will be determined only by the amplitude sampled at time  $t$  and a random increment  $s(u) = w(t+u) - w(t)$ . The covariance is given by

$$\begin{aligned} \text{Cov}[w(t), w(t+u)] &= \int_{w(t)} \int_{w(t+u)} [w(t) - \bar{w}(t)][w(t+u) - \bar{w}(t+u)] \\ &\quad \times p[w(t), Q(t+u)] dw(t) dw(t+u) \\ &= \int_{w(t)} [w(t) - \bar{w}(t)] dw(t) \int_{s(u)} [s(u) - \bar{s}(u)] ds(u) \\ &= \int_{w(t)} [w(t) - \bar{w}(t)] dw(t) [w(t) - \bar{w}(t)] \end{aligned}$$

$$= \int_{w(t)} [w(t) - \bar{w}(t)]^2 dw(t) = \text{Var}[w(t)]. \quad (12)$$

From measured data, one can determine the electronic noise amplitude and the diagonal terms of  $\Sigma_{\text{total}}$ . From this, the diagonal terms of  $\Sigma_{\text{transport}}$  are given by

$$\text{diag}[\Sigma_{\text{transport}}] = \text{diag}[\Sigma_{\text{total}}] - \text{diag}[\Sigma_{\text{electronic}}]. \quad (13)$$

Using Eqs. (12) and (13), we can derive an approximated covariance matrix  $\Sigma_{\text{total}}$  as shown in Fig. 8. A column of the covariance matrix is compared with the experimentally measured one in Fig. 9. The columns compared are corresponding to the waveform amplitude sampled at 128 ns after the interaction. It showed a reasonable agreement between the measured and predicted covariance entries.

### 3.2.3. Measured timing resolution

The best timing resolution, with full-energy events, was achieved at a depth close to the cathode ( $C/A \in [0.9, 0.95]$ ). The measured timing spectrum has a fairly Gaussian shaped peak of  $\sim 7$  ns FWHM (Fig. 10). For all detected 511 keV events, there is a gradual degradation of timing resolution with decreasing interaction depth, as

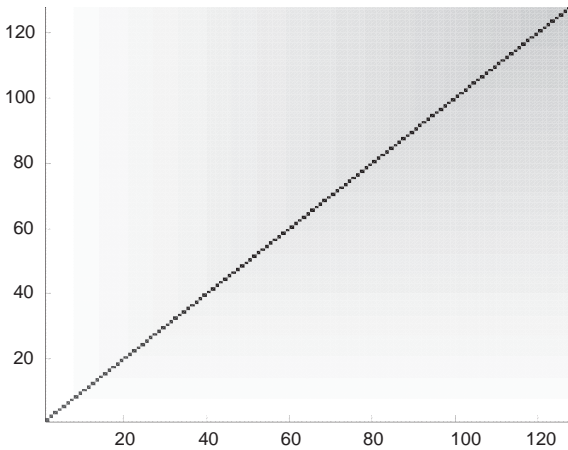


Fig. 8. Approximated covariance matrix for waveform section corresponding to the first 128 ns after interaction.

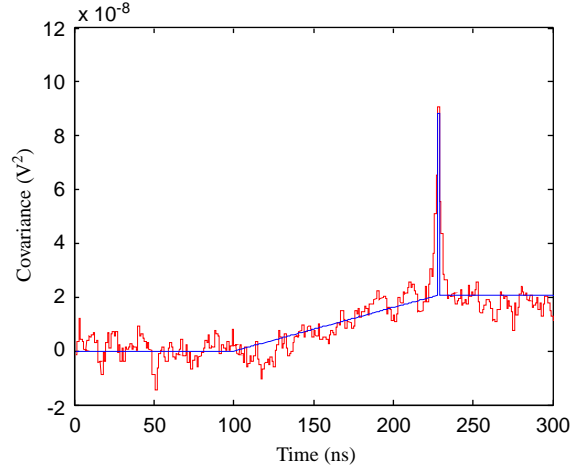


Fig. 9. Comparing measured and approximated columns of the covariance matrix. The solid line shows approximated covariance entries and the dotted curve represents measured values.

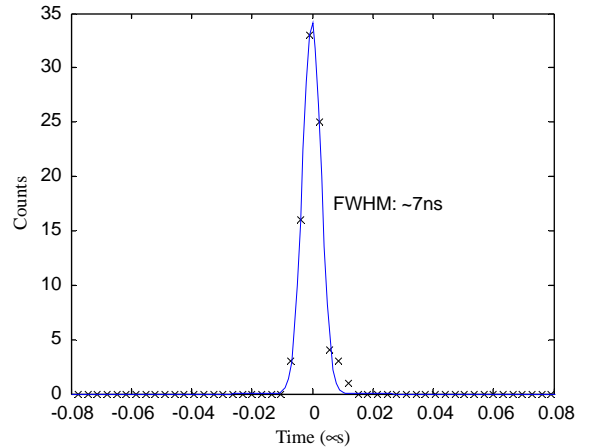


Fig. 10. Measured timing resolution with full-energy events at CAR of  $\sim 0.9$ .

shown in Fig. 11. This results in an overall timing resolution of  $\sim 9.5$  ns for all detected full-energy events. This timing spectrum also has longer tails when compared with that for full-energy events at a specific depth (as shown in Fig. 10). The timing resolution measured with all events having an energy deposition greater than 250 keV is 11.6 ns. These results are shown in Figs. 12 and 13.

We compared these results with those achieved by fitting the measured waveforms to Hecht



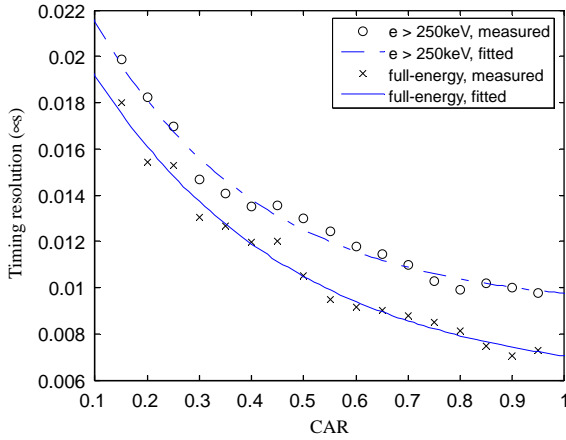


Fig. 11. Measured timing resolution as a function of interaction depth (CAR) with full energy events (crosses) and events having energy deposition  $>250$  keV (circles).

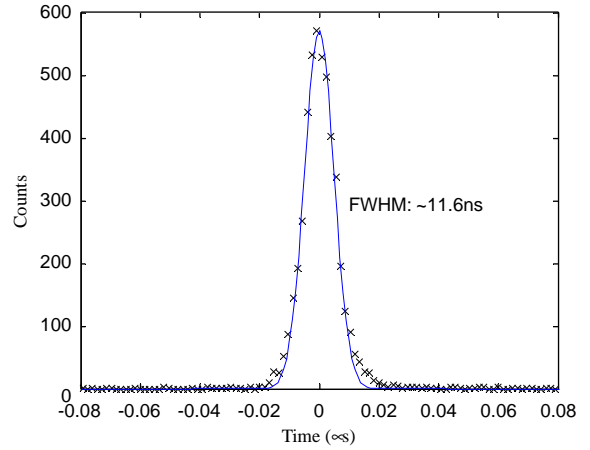


Fig. 13. Measured timing resolution with all events having energy deposition greater than 250 keV and  $CAR \in [0.1, 1.0]$ .

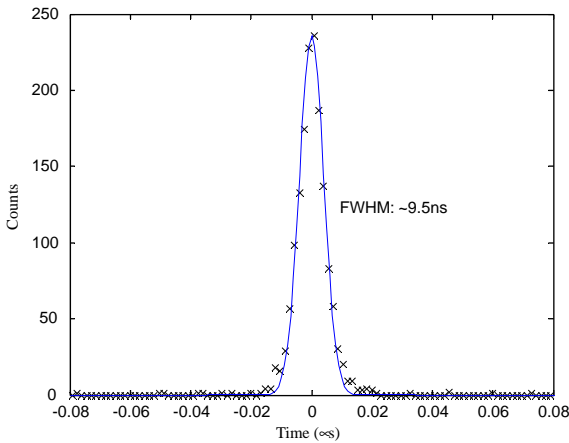


Fig. 12. Measured timing resolution with full energy events and  $CAR \in [0.1, 1.0]$ .

relation (the single exponential model in Table 1). The use of the “optimum” waveform model resulted in better accuracy for timing estimation as shown in Table 2. This improvement is due to the following reasons: (a) the experimentally measured waveform model better describes the actual shape of the waveforms and therefore reduced systematic errors, (b) the use of a correct covariance matrix improved fitting accuracy and (c) numerically, the use of a more accurate system model improves the condition of the inverse

Table 2

Comparing timing resolution achieved with different waveform models

	Optimum model (ns)	Hecht relation (ns)
$C/A \in [0.8, 0.85]$	8.0	9.2
Full energy		
$C/A \in [0.8, 0.85]$	9.7	10.8
$E > 250$ keV		
$C/A \in [0.1, 1.0]$	9.5	11.4
Full energy		
$C/A \in [0.1, 1.0]$	11.6	13.1
$E > 250$ keV		

problem and reduces the possibility that the fitting process converges to a local extrema, which is not necessarily the global ML solution for this timing estimation problem. As we see in practice, this also improved the speed of convergence.

Compton scattering of gamma-rays inside the detector may result in multiple interaction sites for a single event. At 511 keV, we expect these events to account for more than 50% of all detected events. Using the 3-D position sensing technique, we can identify these events in real time. Locations and energy depositions of these multiple interaction sites can be derived precisely. Therefore, a straightforward approach, for treating a Compton

scattered event, is to “synthesize” an expected waveform based on the detailed information regarding all simultaneous interactions and then fitting the measured waveform to the “synthesized” mean waveform to find the interaction timing. Furthermore, since majority of Compton scattered events would have their multiple interaction sites relatively close to each other, the actual waveforms for these events will be close to that resulted from single-site interactions. In this case, we may expect that a reasonable timing accuracy can be achieved by treating these events as single interaction events. The effect of inter-detector Compton scattered events will be studied in our future work.

### 3.2.4. Limiting timing resolution

The minimum achievable error for timing estimation using the “optimum” model was calculated and compared with experimental measurements with full-energy events at several discrete depths. The results are shown in Table 3. The experimentally measured timing resolutions are reasonably close to the theoretical predictions, especially when considering the contribution from the BaF<sub>2</sub> coincident detector. These results indicate that the timing resolution achieved using the “optimum” model is close to the limiting performance that can be obtained with current detector configuration. Further improvement can only be achieved with (a) detectors with higher bias or smaller depth for greater charge drifting velocities and (b) lower readout electronics noise and (c) improved material property and internal electric

field configurations that have reduced fluctuation in charge transport process.

### 3.2.5. Limiting event rate

In this approach, the interaction timing is derived by matching the measured waveform to an expected one using iterative least-square fitting methods. If the number of data points in the waveform is  $n$ , the number of model parameters is  $m$  and in average  $l$  iterations are used to reach convergence, the total number of floating-point operations required in the fitting is at the order of  $\sim 2 \times m \times n \times l$ . For the detector tested, we see, in practice, that  $m \leq 200$ ,  $l \leq 10$  and three model parameters ( $n = 3$ ). So the total number of floating-point operations required per event is at the order of 12 000. For a single CPU capable of performing 1 G floating-point operations per second, it should be able to handle the computation corresponding to  $\sim 10^5$  events per second. Consider other computational overhead necessary for the fitting, we would expect that such a CPU could handle an event rate of  $> 10^4$  per second. Note that when such detector is used in a PET system, least-square fittings will be performed only to events for which both interactions fall into pre-selected energy windows. Furthermore, one can use analogue triggering signals from anode pixels to pick up only those events that have their two interactions falling into a timing window of  $< 100$  ns in width. This pre-selection procedure was discussed in detail in Ref. [3], which further reduces the number of fitting processes required.

## 4. Conclusions and discussions

We explored the limiting timing resolution that can be achieved with a 1 cm<sup>3</sup> CZT detector. The timing estimation process is treated as a model-fitting problem, in which the data is a multivariate Gaussian random variable with known mean and covariance. Some results from this work are summarized as below:

- A detailed detector response function was derived based on experimentally measured data. This model allows one to account for effects

Table 3  
Comparing experimentally measured timing resolution with theoretical optimum results

	Exp. measured (ns)	CRB (ns)
$C/A \in [0.9, 0.95]$	7.2	6.1
Full energy		
$C/A \in [0.6, 0.65]$	9.4	6.8
Full energy		
$C/A \in [0.4, 0.45]$	11.8	9.7
Full energy		

such as irregular weighting potential function, non-uniformity of internal electric field and non-uniformity of detector material. The use of this system model results in an improved accuracy for timing estimation.

- One can simplify the fitting process by using the combination of CAR and anode signal amplitude as an index, which points directly to the most likely waveform model. This helped to speed up the fitting process and improve the accuracy for timing estimation.
- The measured timing resolution was 9.5 ns for full-energy events and 11.5 ns for all events with energy deposition greater than 250 keV.
- Experimental results were compared with the theoretically predicated optimum performance. This indicated that a limiting timing resolution for this detector configuration is  $\sim 10$  ns for detecting 511 keV gamma-rays.
- Further improvements would require one to optimize the detector hardware for timing estimation. This includes lowering readout electronic noise, using higher bias or smaller detector thickness and improving the detector material non-uniformity, etc.

## References

- [1] F. Zhang, Z. He, D. Xu, G.F. Knoll, D.K. Wehe, J.E. Berry, Improved resolution for 3-D position sensitive CdZnTe spectrometers, *IEEE Trans. Nucl. Sci.* NS-51 (5) (2004) 2427.
- [2] Y.F. Du, Z. He, G.F. Knoll, D.K. Wehe, W. Li, Evaluation of a Compton scattering camera using 3-D position sensitive CdZnTe detectors, *Nucl. Instr. and Meth. A-Accelerators Spectrom. Detectors Assoc. Equip.* 457 (1–2) (2001) 203.
- [3] L.J. Meng, Z. He, Estimate interaction timing in large volume HgI2 detector using cathode pulse waveforms, *Nucl. Instr. and Meth. A* 545 (2005) 234.
- [4] Z. He, G.F. Knoll, D.K. Wehe, J. Miyamoto, Position-sensitive single carrier CdZnTe detectors, *Nucl. Instr. and Meth A* 388 (1–2) (1997) 180.
- [5] <http://www.amptek.com/a250.html>.
- [6] G.F. Knoll, (Ed.), *Radiation detection and measurement*, third ed, Wiley, New York, ISBN0-470-07338-5, 1999.
- [7] Chapter 7 in *Numerical Recipes in C*, Cambridge University Press, Cambridge, ISBN0-521-43720-2.
- [8] H.L. Van Trees, *Detection, Estimation and Modulation Theory*, Wiley, New York, 1968.
- [9] N.H. Clinthorne, N.A. Petrick, W.L. Rogers, A.O. Hero, A fundamental limit on timing performance with scintillation detectors, *IEEE Trans. Nucl. Sci.* 37 (1990) 658.
- [10] A.O. Hero, N.H. Clinthorne, W.L. Rogers, A lower bound on PET timing estimation with pulse pileup, *IEEE Trans. Nucl. Sci.* 38 (1991) 709.